Characterization of the plasma current quench during disruptions in the National Spherical Torus Experiment

S.P. Gerhardt, J.E. Menard and the NSTX Team

Princeton Plasma Physics Laboratory, Plainsboro, NJ, USA

Abstract

A detailed analysis of the plasma current quench in the National Spherical Torus Experiment (Ono *et al* 2000 *Nucl. Fusion* **40** 557) is presented. The fastest current quenches are fit better by a linear waveform than an exponential one. Area-normalized current quench times down to $0.4\,\mathrm{ms\,m^{-2}}$ have been observed, compared with the minimum of the $1.7\,\mathrm{ms\,m^{-2}}$ recommendation based on conventional aspect ratio tokamaks; as noted in previous ITPA studies, the difference can be explained by the reduced self-inductance at low aspect ratio and high elongation. The maximum instantaneous $\mathrm{d}I_{\mathrm{P}}/\mathrm{d}t$ is often many times larger than the mean quench rate, and the plasma current before the disruption is often substantially less than the flat-top value. The poloidal field time derivative during the disruption, which is directly responsible for driving eddy currents, has been recorded at various locations around the vessel. The I_{P} quench rate, plasma motion and magnetic geometry all play important roles in determining the rate of poloidal field change.

PACS numbers: 52.55.Fa

1. Introduction

In order to be economically viable, a tokamak [1] fusion reactor must operate with high reliability. This reliability is threatened by a phenomenon known as a major disruption, where the plasma stored energy is rapidly lost, followed by an immediate termination of the plasma current. This process not only terminates the power-generating fusion reactions but can also lead to potentially damaging electromagnetic [2] and thermal loading on in-vessel components. An excellent summary of disruption physics and consequences can be found in [3].

A typical disruption passes through three phases. The first phase occurs when some event, often related to a magnetohydrodynamic instability, causes a degradation of confinement. A large fraction of the stored energy [4], and possibly some smaller fraction of the toroidal plasma current, is typically lost during this phase. At some subsequent point, the remaining thermal energy of the plasma is rapidly lost, typically on a time-scale of $\leqslant 1\,\mathrm{ms}$; this is known as the thermal quench. The thermal loading on the plasma facing components during this phase can be quite severe, with significant melting and vaporization of component surfaces expected in a reactor grade plasma [5]. Because the remaining cold plasma is quite resistive, the toroidal current rapidly decays in the final current quench phase [6, 7], sometimes with a conversion of a fraction

of the plasma current to a runaway electron beam [8–10]. The large magnetic flux changes during this current quench can drive eddy currents in nearby conduction structures, resulting in large $J \times B$ forces and torques on those structures. It is the purpose of this paper to describe the current quench in the spherical torus (ST) plasmas [11] of the National Spherical Torus Experiment (NSTX) (figure 1) [12].

To understand the deleterious effects of a rapid current quench, consider the evolution equation for the current (I) inductively driven in an in-vessel component during a current quench [6]:

$$\frac{\mathrm{d}I}{\mathrm{d}t} + \frac{I}{t_{\mathrm{c}}} = -\frac{1}{L}\frac{\mathrm{d}\Phi}{\mathrm{d}t}. \qquad (1)$$

Here, t_{c} is the L/R time of the current path in the component and L is the inductance of that current path. Φ is the magnetic flux through the component, which changes in time due to changes in both the plasma current magnitude and the position (and changes in the coil currents as well). For structures with time constants t_{c} short compared with the $I_{\mathrm{P}}(t)$ quench time, the induced current is proportional to the instantaneous flux change. For structures with time constants much longer than the current quench, the induced current is proportional to the total flux change. Thus, it is important to assess the waveform of the fastest current quenches. For instance, for
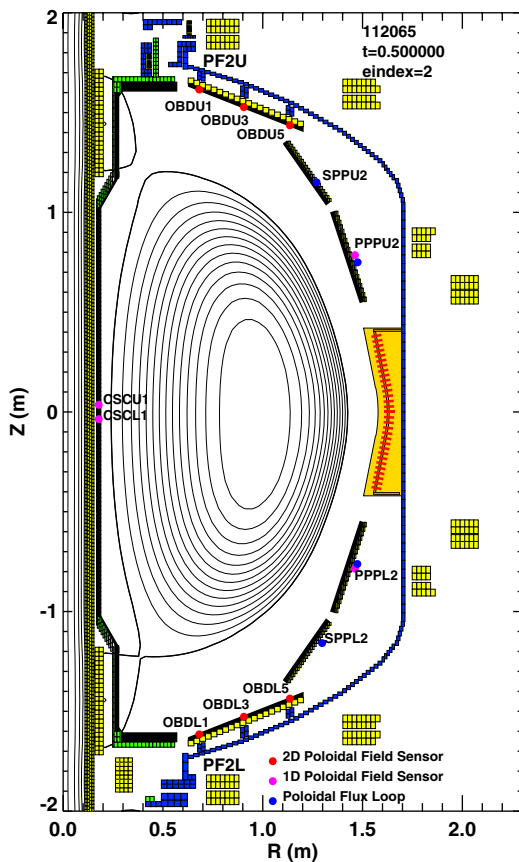
Figure 1. Schematic of the NSTX along with the sensors used in this study. The plasma current is in the plane of the figure, the dominant vertical field points down and the toroidal field points out of the plane. The equilibrium is for discharge 112065, which had the fastest ever current quench in the NSTX with $QR_{(80-20)} = 1050 \, \mathrm{MA\,s^{-1}}$.

a current decay of a fixed total duration, a linear decay will have uniform eddy-current induction, whereas an exponential decay will have the largest induction, at the beginning of the quench. Said another way, it is important to assess the fastest instantaneous quench rates as well as the average quench rates. Furthermore, the magnetic flux linking the component (Φ) is a function of both the plasma current and the magnetic geometry; it is thus important to assess how the geometry of the device and the plasma position dynamics, in addition to the $I_{\mathrm{P}}(t)$ quench rate, impact the time derivative of the linked flux. As an example of the importance of these dynamics, it was shown [5] that eddy currents driven in blanket modules in ITER (see [13] and references therein) provide the main electromagnetic loading during fast current quenches and that the design at the time of that modelling had little safety margin on these loads.

The ST is similar to a tokamak, but in the limit of a very low aspect ratio. This seemingly simple modification to the geometry leads to many attractive features [11], including higher natural elongation and significantly higher MHD stability limits [14]. However, ST plasmas are not immune to disruptions; indeed, as will be discussed below, they often have faster current quenches than conventional aspect ratio tokamaks. Hence, to enable the robust design of future ST devices, it is necessary to assess the detailed

characteristics of disruptions, including the current quench. Of particular importance is to determine where the results from the conventional aspect ratio extend to the ST and where there are differences that can be ascribed to the geometry of the ST. The NSTX is an appropriate device to execute these studies, capable of operating at very high-β [15] and with a wide range of plasma shapes [16].

This paper addresses the dynamics of the current quench process in the NSTX, for a wide variety of disruptions observed over seven years of operations. A description of the NSTX device, diagnostics and disruption database is given in section 2. A brief discussion of five disruption $I_{\mathrm{P}}(t)$ waveforms is given in section 3. It is shown that the waveforms for the fastest current quenches are more accurately fit by linear current decays than exponential, though neither is a good fit in many somewhat slower cases. Section 4 presents database analysis of the current quench rates. Current quench rates up to $1000 \, \mathrm{MA\,s^{-1}}$ have been observed, with events in the range of $300 \, \mathrm{MA\,s^{-1}}$ reasonably common; the maximum current quench rate is often two to four times the average quench rate. As previously described in [17], the fastest current quenches in the NSTX (on an area normalized basis) are substantially faster than for conventional aspect ratio devices; a plausible explanation for this is given in terms of the effective inductance of the plasma, which is smaller for a low aspect ratio and higher elongation. Section 5 describes the relationship between, on the one hand, the current quench rate, plasma current magnitude, plasma motion and magnetic geometry and, on the other hand, the time variation of the local poloidal field and induced eddy currents at various locations around the device. It is shown that the plasma inward motion during the thermal quench or vertical motion during a vertical displacement event (VDE) can drive large field time variations and eddy currents and that the plasma geometry can also have a significant effect. A summary is provided in section 6.

Note that halo currents can provide an additional source of electromagnetic loading on in-vessel structures [18–23]. These currents occur when the plasma becomes vertically unstable and comes in contact with in-vessel components; currents flow directly between the outer 'halo' region of the plasma and those components. The resulting $J \times B$ force on in-vessel components can be as severe as that from quench-induced eddy currents. Results from halo current measurements in the NSTX will be presented in a future publication.

2. Diagnostics and methods

A database of disruptions in the NSTX has been created in order to execute this analysis. The quantities stored in the database largely conform to the variables set up for the ITPA disruption database [17]. However, additional specific quantities are also recorded, such as the poloidal field time variation at specific places in the device, additional parametrizations of the current quench and additional measures of the plasma vertical motion. The time of the disruption is automatically determined using an algorithm which brackets the disruption, determines when the disruption starts and calculates the current quench related properties described

below. As described in sections 3 and 4, the plasma current waveform, denoted $I_P(t)$ in this paper, can have a number of drops and spikes at the end of the discharge; the algorithm finds the final large current quench, ignoring earlier, slower decay phases. The times where the plasma current decays to 90%, 80%, 70%, ..., 20% and 10% of the pre-disruption current are recorded (and denoted t_{90}, t_{80}, ..., t_{20} and t_{10}) and the 80–20% quench rate is defined as

$$QR_{(80\text{--}20)} = -\frac{0.6 \times I_{PD}}{t_{20} - t_{80}}. \tag{2}$$

Here, I_{PD} is the plasma current just before the pre-disruption current spike and may be significantly less than the current at the 'representative time', denoted I_P here (see below for more details). The minus sign is specified to make $QR_{(80\text{--}20)}$ a positive number. The current quench time is defined as [17]

$$\tau_{CQ} = \tfrac{5}{3}(t_{20} - t_{80}). \tag{3}$$

Additionally, the plasma current evolution between t_{90} and t_{20} has been fit to both a straight line and an exponential of the form

$$I_{P,\text{ExpFit}}(t) = A_o e^{-(t-A_1)/\tau_D}. \tag{4}$$

The maximum time derivative of $I_P(t)$ is also recorded, defined as $(dI_P/dt)_{\max} = \max(|dI_P/dt|)$, which is positive definite.

The plasma current is measured by a Rogowski coil located outside the vacuum vessel. As described in [24], the voltages on many toroidal loops fixed to the vacuum vessel surface are used to infer the vessel currents, which are then subtracted from the Rogowski measurement. However, as will be apparent below, the compensation shows a small error on the time-scale of the fastest current quenches, with the measured $I_P(t)$ often slightly negative for a brief period at the end of the quench; this slight error does not impact any of the conclusions presented here. Approximately 70 Mirnov coils and 40 poloidal flux loops are located around the plasma boundary to measure the equilibrium poloidal magnetic field and the flux. Many of the Mirnov sensor locations near the top and the bottom of the machine are instrumented to measure the poloidal field both tangent and normal to the plasma boundary, while those closer to the midplane typically measure only the tangent field. All sensors are analog integrated and then digitized at 5 kHz. The data from the Mirnov coils, poloidal flux loops and $I_P(t)$ Rogowski are smoothed with a 3-point boxcar average before processing for inclusion in the database.

In addition to the magnetics data, many parameters from the equilibrium code EFIT [25] are stored in the database. These EFIT reconstructions are generally available for every discharge, with 5 ms time steps. The parameters are generally stored in the database at the final good equilibrium time-slice before the disruption, denoted by a subscript D (as long as it is within 10 ms of the disruption starting), and at a 'representative time', which is taken for this study to be the time of the maximum stored energy. Note that it is thus possible for the pre-disruption current to be larger than the 'representative current'. Stored quantities relevant to this study include the cross-sectional area (A, A_D), elongation (κ, κ_D), lower triangularity (δ_l, δ_{lD}) and cylindrical safety factor (q^*, q_D^*), defined as $q^* = \varepsilon(1 + \kappa^2)(\pi a B_T / \mu_0 I_P)$ [14].

The ∼938 shots in this database are taken from the 2002–2008 run campaigns and are chosen to include

- all NSTX discharges with $|QR_{(80\text{--}20)}| > 2.5 \times 10^8$ A s^{-1},
- the 100 NSTX discharges with the largest ratio of $(dI_P/dt)_{\max}$ to $QR_{(80\text{--}20)}$,
- all discharges with a pre-disruption stored energy greater than 125 kJ,
- all discharges with halo currents >40 kA during the FY 2008 campaign.

Additionally, a large number of nominally 'interesting' disruptions were included, even if they did not make it to the top of one of these ranking categories. This selection of shots contains a large variety of discharge parameters and disruptions, caused by many different types of MHD activities (locked modes, intentional and inadvertent VDEs, excessive pressure peaking disruptions, resistive wall modes). It is not, however, representative of a random sample of all discharges in the NSTX, nor necessarily a random sample of all disruptions.

It is also important to note that the NSTX control system [26] neither detects nor attempts to mitigate disruptions. In many cases, an MHD event causes the loss of a large fraction of the stored energy and a smaller loss of the plasma current (and, if the plasma is in H-mode before that time, loss of the edge pedestal as well). The $I_P(t)$ feedback controller will then demand a maximum loop voltage (∼5 V, depending on the solenoid current level) in order to sustain the plasma current, up to the -24 kA current limit on the solenoid. Vertical stability is quite often lost during this phase, which typically has a higher internal inductance due to loss of the pedestal and the rapid current penetration in the colder plasma. The final thermal and current quenches occur when either the plasma makes contact with divertor or the loop voltage is reduced to zero at the solenoid coil current limit. This common case is thus intermediate between a true hot-plasma VDE, where the plasma stored energy is high before the vertical motion begins, and a typical vertically unstable disruption, where the vertical motion begins after the thermal quench[1]. In other cases, the event precipitating the disruption is sufficiently severe that the plasma current decays to zero before the I_P feedback controller can respond. As there is typically no detrimental effect for the next discharge after a disruption for present NSTX parameters, no attempt is made to restrict the heating power, deshape the plasma, move it to a neutral point [27, 28], ramp the plasma current down or otherwise soft-terminate the discharge.

3. Current quench rates and $I_P(t)$ waveforms

Before presenting the database analysis, it is instructive to consider the detailed $I_P(t)$ waveforms for the five quenches in figure 2. In each case, the time of the disruption is indicated by a black vertical line, the best-fit linear waveform (between t_{90} and t_{20}) by a blue line and the line tangent to the waveform at the point of maximum dI_P/dt in magenta. Some parameters related to the current decay are indicated in each frame as well.

---

[1] For discharges whose shape is controlled by the Isoflux algorithm [29] during the I_P flat-top, a dynamic change is made to a simple gap-control algorithm when the plasma current drops below 200 kA. The mismatch between the actual and requested shapes at this transition is usually severe, exacerbating the control problems of the disrupting plasma.
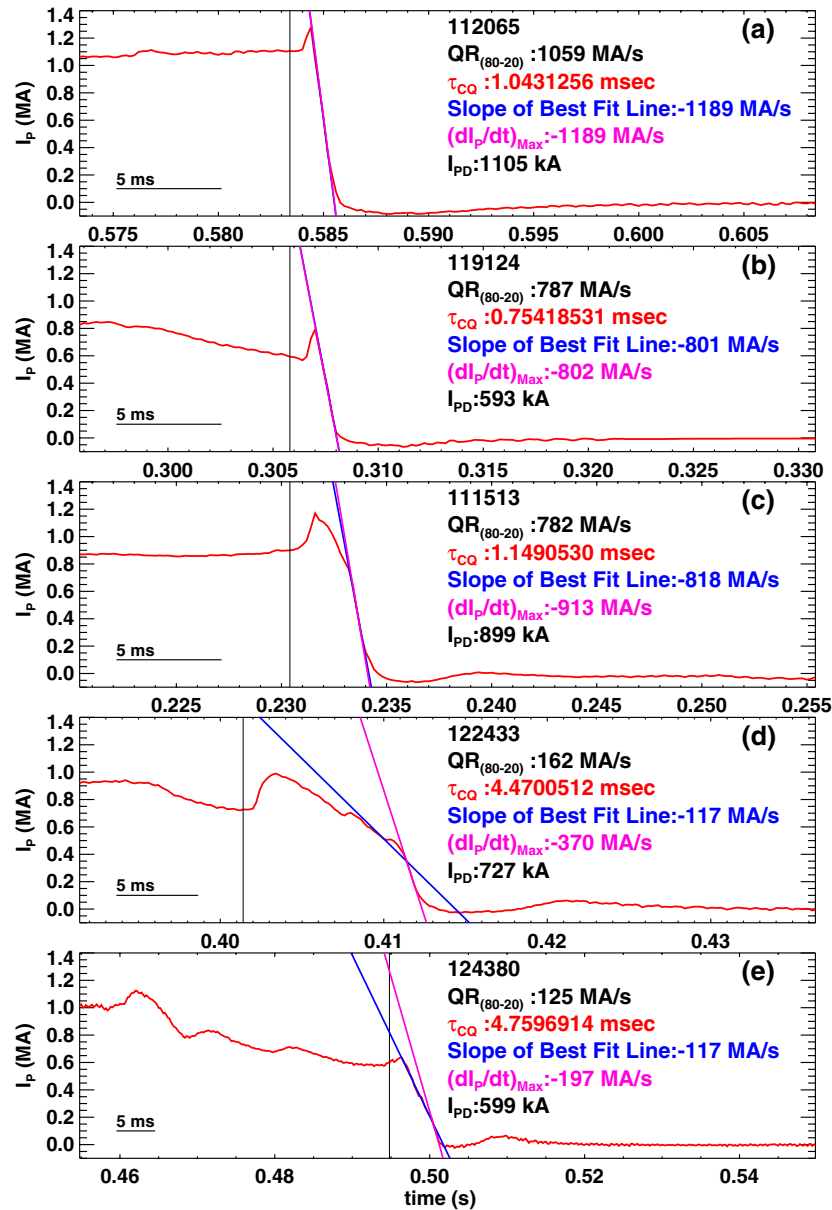
Figure 2. Waveforms of the I_P decay for five disruptions: (*a*)–(*c*) shots 112065, 119124 and 111513, which had the three fastest I_P quenches in the NSTX database, (*d*) shot 122433, which shows a slower initial decay phase followed by a rapid quench, and (*e*) shot 124380, a case where the pre-disruption plasma current is significantly less than that during the I_P flat-top. The linear fit is shown in blue in all cases, and the line tangent to the point of maximum quench rate is shown in magenta. Note the 5 ms long bar in the lower left of each frame used to indicate the different time-scales.

The time duration enclosed within each frame is not the same; a horizontal line 5 ms long is drawn at the bottom left of each frame in order to indicate the relative time-scales. Note that all but one case here, and in general most disruptions in the NSTX, show a sharp rise in the plasma current before the I_P quench. This rise is required in order to conserve magnetic energy during the flattening of the current profile associated with the thermal quench [1].

The first three frames of figure 2 show the fastest three current quenches in the NSTX database (using the 80–20% criterion); that in frame (*a*) is the fastest quench in the database. This discharge achieved $\beta_N = 6$, before a large rotating $n = 1$ instability grew, resulting in a loss of stored energy and an increase in the internal inductance. This in turn caused the

discharge to become inner-wall limited, after which it fell out of H-mode. The pressure peaking then increased dramatically, and the discharge disrupted. The case in figure 2(*b*), discharge 119124, develops a locked mode at $t = 0.25$, causing a near-total loss of stored energy. The I_P controller is able to hold the plasma current until $t = 0.3$, when the loop voltage goes to zero and the final current quench occurs. The plasma stays centred and is limited on the centre column through the locked mode and disruption. Although there are less diagnostic data available for the discharge in figure 2(*c*) (111513), equilibrium reconstructions show it to become inner-wall limited during the current ramp just before the fast quench.

The final two frames in figure 2 illustrate current quenches that are not among the very fastest, but that illustrate interesting

features. The waveform in figure 2(*d*) shows a case where the maximum quench rate is 2.3 times larger than the 80–20% quench rate. While the diagnostic information is limited for this discharge, it appears that a locked mode causes the initial loss of stored energy and vertical position control. The final rapid thermal and current quenches occur after the plasma comes in contact with the lower outboard divertor at $t \approx 0.405$. The current quench begins relatively slowly, but accelerates with time to a $(dI_p/dt)_{max}$ of $\sim370\,\mathrm{MA\,s^{-1}}$. The discharge in figure 2(*e*) illustrates a case where the plasma current just before the quench (I_{PD}) is substantially smaller than that during the representative flat-top time (I_P). In this case, a magnetic signature typical of an RWM is seen on the large-area external mode sensors [30], followed by a rapid loss of confinement and loss of vertical position control. The loop voltage is then increased to ≈4.5 V by the I_P feedback controller, although this value is insufficient to achieve the requested 1 MA in the cold resistive plasma and the toroidal plasma current continues to decrease. The final thermal and current quenches occur when, after a period of oscillations, the vertical motion of the plasma brings it in contact with the secondary passive plates as the bottom of the device at $t \approx 0.495$.

We have fit NSTX current waveforms to both linear and exponential decay waveforms, using the same methodology as described in Sugihara *et al* [6]. We find that in general, the linear decay is a better fit than the exponential waveform for the very fastest current quenches, implying a uniform (in time) eddy-current drive; this is to be anticipated from the waveforms in, for instance, figures 2(*a*)–(*c*). The fastest current quenches do not have an 'S' curve $I_P(t)$, as was noted to be common in the 1998 ITER Physics baseline [31]. In JET [7] and JT-60 [6], an exponential waveform was often a good fit to the fastest current quenches; the fit was attributed to the presence of a runaway electron tail [32]. No runaway tail is typically observed in NSTX disruptions, which may account for this difference between the various machines. However, neither waveform is in general representative of the fast current quenches in NSTX. Multiple slopes in the $I_P(t)$ waveform are common and not fit well by either of these approximations. These multiple slopes will give rise to often large differences between $QR_{(80-20)}$ and the $(dI_P/dt)_{max}$.

4. Database analysis of current quench rates in the NSTX

As discussed above and in [17], the 80–20% quench rate, denoted here as $QR_{(80-20)}$, has become a generally accepted metric for the quench rate. A scatter plot of $QR_{(80-20)}$, plotted against the pre-disruption current density (I_{PD}/A_D, in MA m^2), is shown in figure 3(*a*). Discharges that disrupt during the current ramp are shown in red, while those that disrupt during the flat-top or $I_P(t)$ ramp-down are shown in blue[2]. The plot illustrates that quench rates in the range of 400–700 MA s^{-1} have occurred in many instances over the 8 year time span included in the database. Note that the quench

2 In order to automate the determination of when the disruption occurred, the shot is considered to have disrupted on the $I_P(t)$ ramp if all of the following requirements are fulfilled (i) the disruption occurred before 0.3 s, (ii) dI_P/dt at 40 ms before the disruption was greater than 2 MA s^{-1} and the loop voltage 40 ms before the disruption was greater than 0.5 V.
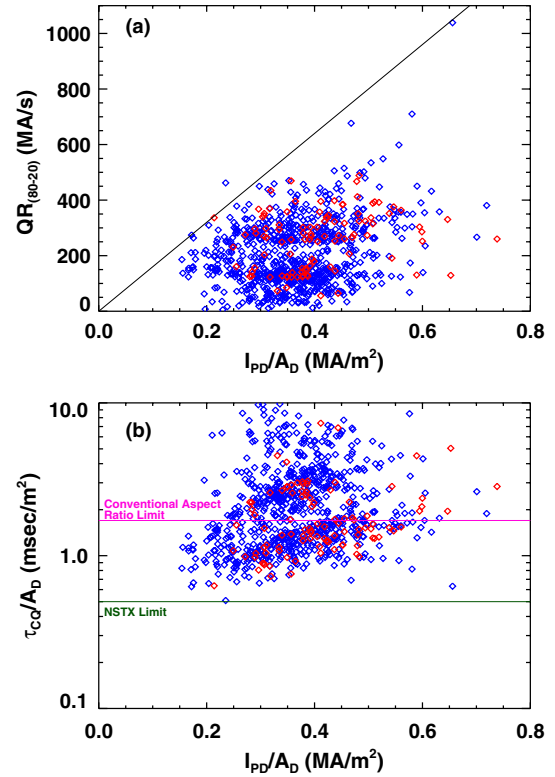

Figure 3. (*a*) The 80–20% quench rate and (*b*) the area-normalized quench time, both plotted against the average current density during the equilibrium time. Red points correspond to disruptions during the current ramp, while blue points indicate disruptions during the $I_P(t)$ flat-top or ramp-down.

rate is apparently bounded by the line $1600I_{PD}/A_D$, with I_{PD} in MA and A_D in m^2. Cases that disrupt both during the ramp and during the flat-top approach this boundary line.

The same data are shown in figure 3(*b*), in this case as τ_{CQ} normalized to the pre-disruption cross-sectional area. In this case, the minimum quench times are 0.5 ms m^{-2} or ~1 ms for a typical 2 m^2 NSTX plasma, consistent with the waveforms in figures 2(*a*)–(*c*). This area-normalized time can be compared with the recommendation of a minimum quench time of 1.7 ms m^{-2} for conventional aspect ratio tokamaks, as given in the 2007 Revised ITER Physics Basis [3] and based upon results from ASDEX-U, ALCATOR C-MOD, DIII-D, JET and JT-60U. Thus, the fastest current quenches in the NSTX, when normalized to the plasma area, are ≈4 times faster than in conventional tokamaks [17].

Normalizing the quench time to the plasma cross-section is physically meaningful if the current quench is determined by the L/R time of the cold plasma. Taking $\tau_{L/R} = L_P^{eff}/R_P$ with the plasma resistance $R_P = 2\pi\eta R_0/A$, the cross sectional area A and the effective inductance $L_P^{eff} = \mu_0 R_0[\ln(8/\sqrt{\kappa}\varepsilon) - 7/4]$, the area normalized decay time becomes

$$\frac{\tau_{L/R}}{A} = \frac{\mu_0}{2\pi\eta}\left[\ln\left(\frac{8}{\sqrt{\kappa}\varepsilon}\right) - \frac{7}{4}\right], \tag{5}$$

depending on only the aspect ratio (logarithmically) and the plasma resistivity (η). The factor in brackets evaluates to 1.2 at a conventional aspect ratio ($\varepsilon = r/R = 1/3$, elongation $\kappa = 1.6$) and to 0.25 for typical NSTX parameters
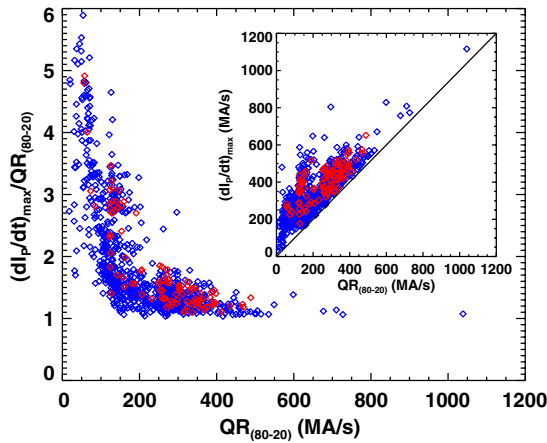
Figure 4. The ratio of $(dI_P/dt)_{max}$ to $QR_{(80-20)}$, plotted against $QR_{(80-20)}$. Also shown in the inset is $(dI_P/dt)_{max}$ versus $QR_{(80-20)}$.

$(\varepsilon = r/R = 0.75, \kappa = 2.1)$. Thus, a factor of 4–5 in quench rates $(1.2/0.25 \approx 4.8)$ can be accounted for simply through the aspect ratio and elongation arguments, in line with the difference observed in the data.

Confirmation of this classical L/R current decay model has been seen in DIII-D plasma shut-downs initiated by He gas injection [33], where spectroscopic measurements of the electron temperature and Z_{eff} [34] allowed more precise modelling of the quench dynamics [35]. Note, however, that if the L/R time of a close fitting vessel becomes longer, the aspect ratio effect described above becomes less important; the difference between STs and conventional aspect ratio tokamaks in that limit is then determined by the plasma internal inductance only. Also, recent results from JT-60U [36] have demonstrated that the time evolution of the internal inductance is important in understanding the details of the current decay.

As noted above, it is common for $(dI_P/dt)_{max}$ to exceed $QR_{(80-20)}$. The ratio of these two quantities is plotted against $QR_{(80-20)}$ in figure 4, where the colour scheme is the same as in figure 3. At the highest quench rates, there is little difference between $QR_{(80-20)}$ and $(dI_P/dt)_{max}$; these cases typically have near linear decay waveforms, as illustrated in figures 2(a)–(c). For somewhat slower current quenches, however, the maximum quench rate is often 3–5 times the 80–20% value. Thus, discharges with a $QR_{(80-20)}$ significantly less than the maximum can still pose a threat to components with short time constants. The inset shows the same data, but plotted as $(dI_p/dt)_{max}$ versus $QR_{(80-20)}$. Because the largest ratios $(dI_p/dt)_{max}/QR_{(80-20)}$ occur at fairly low average quench rates, the values of $(dI_p/dt)_{max}$ at those large ratios are only up to $\sim 400\,\text{MA}\,\text{s}^{-1}$.

It was noted in the context of figure 2(e) that the current immediately preceding a disruption is often less than that at the $I_P(t)$ flat-top or time of the maximum stored energy. The ratio of pre-disruption current (I_{PD}) to 'representative time' current (I_P) is shown as a histogram in figure 5, again with current-ramp and flat-top cases in red and blue, respectively. The frequency distributions are normalized to a maximum of 1, although the number of cases in the two categories is different as indicated in the figure. In both cases, there is a maximum in the distribution at $I_P/I_{PD} \approx 1$ and a rather broad distribution for smaller ratios; the distribution tends to be broader for
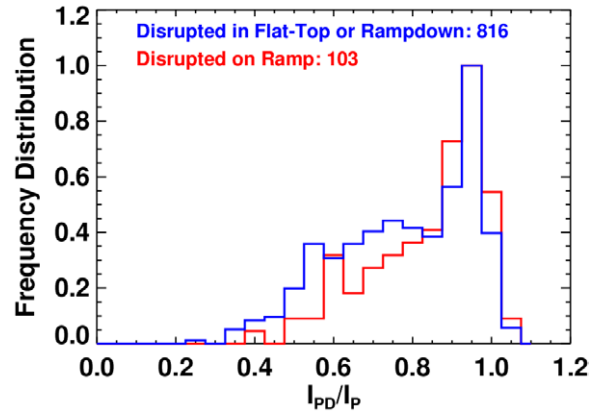

Figure 5. Histogram of the ratio of the pre-disruption current to the representative plasma current.
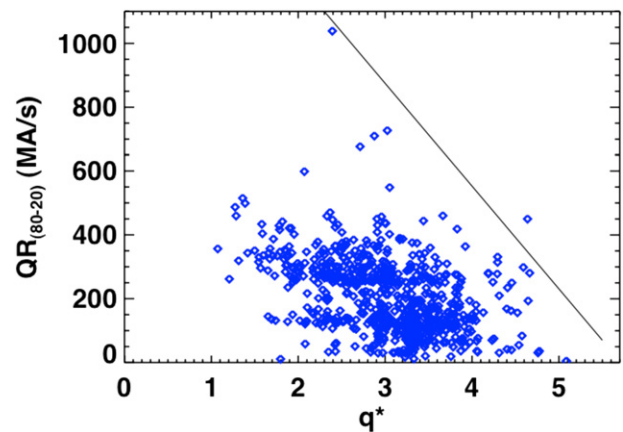

Figure 6. Scatter plot of $QR_{(80-20)}$ as a function of q^* at the representative time.

flat-top disruptions, indicating that they are more likely than ramp-up cases to lose a large fraction of their current during the pre-disruption phase. This may somewhat mitigate the effect of many of these disruptions; however, many fast cases, like 112065 in figure 2(a)) above, disrupt rapidly at full current.

For those discharges that disrupt after the I_P ramp is complete, efforts were made to correlate the quench rate with various discharge parameters such as the stored thermal energy, triangularity, elongation, safety factor and toroidal or normalized β. These efforts were generally unsuccessful, as the fastest current quenches have occurred over a wide range of parameters. This in not necessarily a surprise, as it is often unclear how these equilibrium parameters would impact the plasma resistivity during the quench. However, one weak correlation was found between $QR_{(80-20)}$ and the representative time value of q^*, as illustrated in figure 6. Most of the fastest current quenches occur for $q^* < 3$, and there is a trend of decreasing $QR_{(80-20)}$ with the increase in q^* for $q^* > 3$, as indicated by the line in the figure. The sole point sitting above the line (discharge 111364) became vertically unstable during the $I_P(t)$ flat-top, impacting on the upper divertor with a resulting fast I_P quench. However, many discharges with $q^* < 3$ occur without rapid (or any) disruption, and these data cannot be taken to indicate the recommended q^* operating space. Note that q^* was previously found to be a good aspect

Table 1. Poloidal field sensors utilized in this study.

Sensor locations	Abbreviation	Components measured
Lower outboard divertor, #1, #3 and #5	OBDL1, OBDL3, OBDL5	Tangent and normal poloidal field
Upper outboard divertor, #1, #3 and #5	OBDU1, OBDU3, OBDU5	Tangent and normal poloidal field
Upper primary passive plate #2, near outboard midplane	PPPU2	Tangent poloidal field
Lower primary passive plate #2, near outboard midplane	PPPL2	Tangent poloidal field
Centrestack casing, upper and lower #1, near inboard midplane	CSCU1, CSCL1	Tangent poloidal field

ratio and shape independent figure of merit for assessing the current limit in a tokamak [14]; thus, it may not be surprising to find at least a weak correlation with this parameter.

5. Dependence of the local magnetic field variation and eddy currents on the quench rate, plasma position and plasma motion

As the discussion surrounding equation (1) indicates, the actual eddy-current drive is determined by the change in magnetic flux through the particular in-vessel component. It is clear that the $I_P(t)$ quench rate will be important in determining the local dB/dt. The analysis below will demonstrate that both the plasma motion and the magnetic geometry local to a particular component are also important in this determination.

The local poloidal field time derivative has been assessed at 10 locations indicated in figure 1 and summarized in table 1. The sensors pairs in the upper (OBDU1, OBDU3, OBDU5) and lower (OBDL1, OBDL3, OBDL5) outboard divertors measure the poloidal field both normal and tangent to the divertor plate. The sensors on the inboard midplane centre stack casing (CSCU1, CSCL1) and outboard primary passive plates (PPPL2, PPPU2) only measure the tangent poloidal field (i.e. that component tangent to the plates and the centre column). These sensor locations were chosen for their distribution around the device and long-term reliability. For each location, the mean dB_{pol}/dt during the current quench, as well as the minimum and maximum values of dB_{pol}/dt, was stored in the database. The present report presents a subset of the total results obtained from this study.

We also present below an analysis of currents driven in the passive stabilizing plates. The NSTX has four rows of 1.3 cm thick copper stabilizing plates, with 12 plates per row. The plates nearest the midplane are known as the upper and lower primary passive plates and those nearer the top and bottom as the upper and lower secondary passive plates. Each plate is mechanically and electrically connected to the vessel by stainless steel supports on both (two) sides, so that an approximately axisymmetric toroidal current path exists with current flowing toroidally along the plates, to the vessel through the support, through the vessel a short distance, then to the next plate through its support. The magnitude of this current is determined via the voltage on flux loops mounted on the plates; the location of these loops is indicated by blue dots in figure 1. As described in [24], an equivalent resistance for the plate + support + vessel circuit (R_{plate}) is defined such that $I_{plate} = V_{loop}/R_{plate}$, where V_{loop} is the voltage on the flux loop behind the plate. We have found that the directly measured voltage often saturates our 5 V digitizers during disruptions. Hence, for the following analysis, the
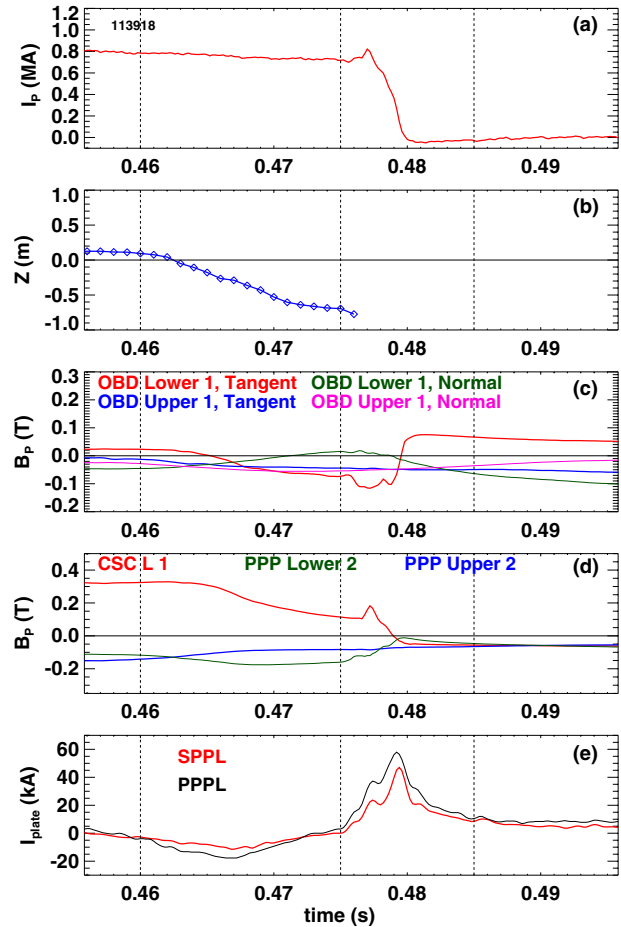

Figure 7. Time traces of (a) the plasma current, (b) the plasma vertical position, (c) the normal and tangent magnetic field traces in the upper and lower outboard divertor, (d) the tangent field near the midplane on the inboard and outboard sides and (e) the currents induced in the lower primary and secondary passive plates. The vertical lines correspond to the times of the reconstructions in figure 8.

hardware-integrated poloidal flux is numerically differentiated to measure the voltage V_{loop}.

The general trends associated with the field evolution for a vertically unstable plasma (discharge #113918) are illustrated in the time traces in figure 7, along with three equilibrium reconstructions for this plasma in figure 8 (vertical stability was lost after a series of internal beta collapses leading to an unsustainable increase in the internal inductance, impeding vertical position control). This discharge has a $QR_{(80–20)} = 365 \text{ MA s}^{-1}$ current quench at $t = 0.477 \text{ s}$, after the plasma has drifted towards and made contact with the lower divertor. There are steady changes in the field magnitudes during the downward drift: the field at the inboard midplane (CSCL1, the
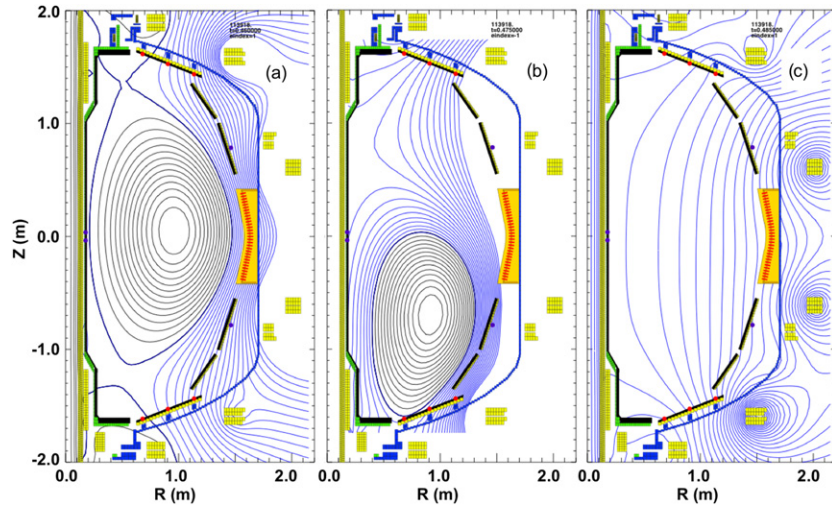
Figure 8. Poloidal flux plots at three times for the discharge illustrated in figure 7. (*a*) $t = 0.46$ s, during the equilibrium phase, (*b*) $t = 0.475$ s, as the downward going plasma is impacting on the lower divertor and (*c*) $t = 0.485$ s, after the current quench. The locations of the B_{pol} sensors are also indicated.

red trace in frame (*d*)) slowly decreases as the plasma drifts down, while the tangent poloidal field at the lower outboard divertor (OBDL1, red trace in frame (*c*)) decreases and even changes sign (positive tangent poloidal field points along the divertor plate and away from the centre column, i.e. to the right and slightly up in the figure). This discharge makes contact with the lower divertor plates at $t \approx 0.47$, after which its cross-section and edge *q*-value continually decrease. When the thermal quench occurs at $t = 0.477$, the plasmas poloidal beta is immediately lost, causing the plasma to shift radially inwards. This in turn causes a sharp increase in the field at the inboard midplane sensor CSCL1. When the current quench occurs, the tangent field at the OBD rapidly becomes positive again, resulting in a very large positive value of $\mathrm{d}B_{\tan}/\mathrm{d}t$. The field at the inboard midplane also decreases to its vacuum value on the time-scale of the current quench.

The process leading to the large values of $\mathrm{d}B_{\tan}/\mathrm{d}t$ at the lower outboard divertor OBDL1 can be seen from the reconstructions in figure 8. At $t = 460$ ms, the sensor location is just inboard of the outer strike point, with the tangent field pointing in the positive *R*-direction. As the plasma moves down and becomes limited on the divertor plate, the private poloidal flux from the plasma links the sensor location, and the tangent poloidal field changes sign. This poloidal field rapidly vanishes once the plasma current quenches. The fields then are simply the vacuum fields due to the PF coils (and any remaining vessel eddy currents) and are again positive at the location of the measurement.

Note that the local field time variations at both the primary passive plates, PPP Lower 2 and PPP Upper 2 in figure 7(*d*), are much smaller than the inboard midplane or the lower divertor. The plasma generally moves away from these locations during the disruption motion, and in general, the local time variations there are small compared with those at the divertor or the inboard midplane. Hence, the poloidal field trends at these locations will not be discussed further in this paper.

The currents in the lower primary and secondary passive stabilizing plates are shown in figure 7(*e*). As the plasma

column drifts down, there is a negative current induced in the plates. This current is in the direction to oppose the plasma vertical motion. The current then returns to zero and becomes positive. Finally, there is a large spike of positive plate currents during the I_P quench. More details regarding the passive plate currents are provided later in this section.

The larger trends of the poloidal field time variations at the lower outboard divertor are shown in figure 9, where the mean $\mathrm{d}B_{\tan}/\mathrm{d}t$ during the current quench is normalized to the plasma current (I_{PD}) and plotted against QR$_{(80-20)}$. The data points are colour-coded according to the vertical position of the plasma at the beginning of the disruption and are thus indicative of the vertical motion that commonly proceeds NSTX disruptions. The vertical position is determined by the 1 ms time resolution equilibrium reconstructions[3], which were not computed for all shots in the database; the number of points is thus reduced compared with the previous figures.

For upward going VDEs (orange, yellow and red points), the I_{PD} normalized $\mathrm{d}B_{\tan}/\mathrm{d}t$ is always near zero: when the plasma moves upwards, the dominant field at the machine bottom is due to the PF coil currents, which do not change appreciably on the fast time-scale of interest. However, as illustrated in figures 7 and 8, the rapid transition from the highly distorted pre-disruption fields to the post-disruption vacuum fields can lead to very large values of $\mathrm{d}B_{\tan}/\mathrm{d}t$ for downward going plasmas. The boundary lines in the figure show that the maximum normalized field variation [mean($\mathrm{d}B_{\tan}/\mathrm{d}t$)]$/I_{PD}$ scales as $C \times$ QR$_{(80-20)}$, where $C = [2.9, 2.3, 1.1]$ T MA^{-2} for sensors [1, 3, 5], respectively. These slopes show that the strongest time variations occur at the innermost sensor, as discussed below.

The data in figure 9 show considerable scatter in the local $\mathrm{d}B/\mathrm{d}t$ values, even when restricted to downward going disruptions only. However, the discussion surrounding figure 7 should make it clear that both the magnetic configuration

---

[3] The 1 ms time-step reconstructions were computed with the LRDFIT equilibrium code, using only magnetic constraints. Only the plasma position was taken from these equilibria; all other quantities are still taken from standard EFIT solutions.
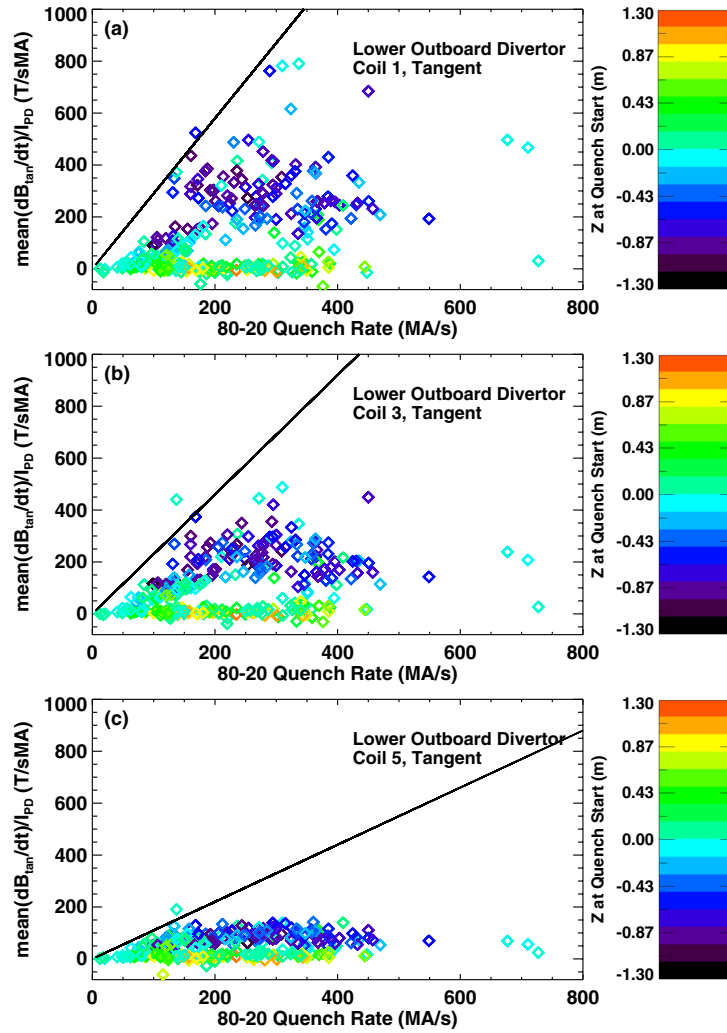
Figure 9. The I_P normalized average dB_{tan}/dt for the three sensor locations in the lower OBD, as a function of the 80–20% quench rate. Colours represent the Z-location of the plasma at the beginning of the disruption.
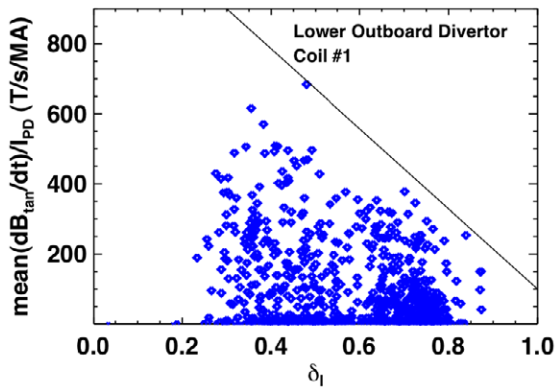

Figure 10. The I_P normalized dB_{tan}/dt at the innermost coil in the lower divertor (OBDL1), as a function of the lower triangularity at the representative time.

near a sensor and the plasma motion have a strong impact on the local field time variation. This point is emphasized in figure 10, illustrating that the envelope of I_{PD} normalized mean (dB_{tan}/dt) values at the OBDL1 sensor is a strong function

of lower triangularity (δ_l) . In order to achieve low values of triangularity at moderate to high elongation, the lower PF2 coil (see figure 1) is operated with current parallel to the plasma current, i.e. there is an attractive force between the coil and the plasma. When the VDE occurs, this attractive force will have a tendency to pull the plasma over the OBDL1 sensor location, leading to the deep reversal of the field and fast transition to the vacuum field after the current quench.

A similar analysis has been done for the upper outboard divertor, with similar results. The I_{PD}-normalized mean(dB/dt) values scale with the quench rate and are larger for smaller values of upper triangularity.

The data in the following two figures imply that among other things, the magnetic geometry and current quench rate are important in determining the local field time variations. An additional contributor is the plasma motion before and during the current quench. For the lower OBD, the downward motion leads to $dB_{tan}/dt < 0$, while the current quench typically leads to $dB_{tan}/dt > 0$. The data in figure 11(*a*) show both the maximum and minimum dB_{tan}/dt, both normalized by I_{PD}, as a function of the $(dI_P/dt)_{max}$ during the quench. The downward
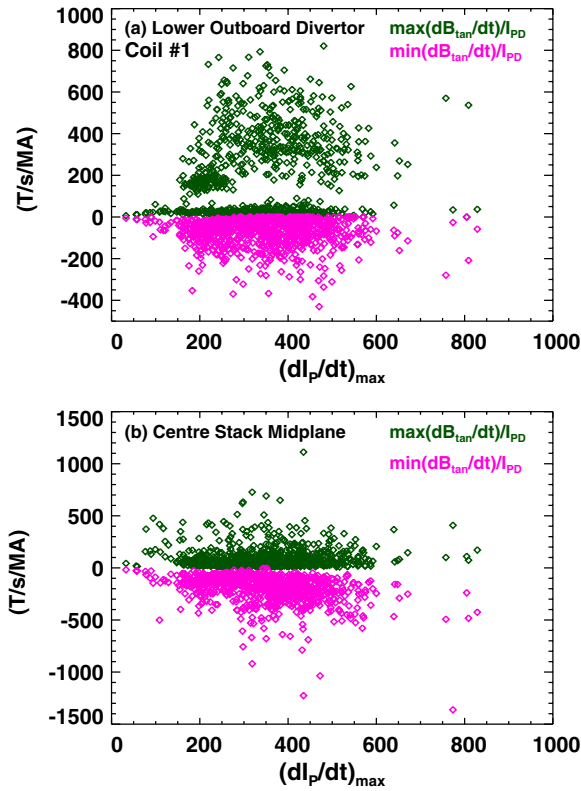
9

Figure 11. The maximum (dark green diamonds) and minimum (magenta squares) I_P normalized dB_{tan}/dt as a function of the maximum dI_P/dt. Data are shown for the innermost lower outboard divertor sensor (OBDL1) in (a) and the inboard midplane sensor (CSCU1) (b).

motion can cause $(dB/dt)/I_{PD}$ values up to $-400\,\mathrm{T\,s^{-1}\,MA^{-1}}$. These values, however, are in absolute magnitude only half of those observed during the quench, where an instantaneous $900\,\mathrm{T\,s^{-1}\,MA^{-1}}$ has been observed. Thus, for this location, the maximum eddy-current loading is due to the quench itself, not the plasma motion, at least for the range of plasma vertical velocities found to date in the NSTX.

The situation is somewhat different at the inboard midplane sensor CSCL1, as demonstrated in figure 11(*b*). The inward shift of the plasma during the thermal quench leads to large positive values of $(dB_{tan}/dt)/I_{PD} \sim 700$–$1000\,\mathrm{T\,s^{-1}\,MA^{-1}}$. These are entirely comparable in magnitude to the most negative values during the current quench, though their time duration is smaller. Hence, the plasma radial motion and current quench can lead to instantaneous eddy-current drive of similar magnitudes. Additional analysis (not shown) has demonstrated that the largest values of $|dB_{tan}/dt|/I_{PD}$ for this location occur in the comparatively rare cases where the plasma remains centred during the current quench, a situation favoured by having low elongation.

Finally, consider the scaling of the disruption-induced passive plate currents with the plasma current. As discussed above, when the plasma has entered a vertically unstable phase and is drifting towards the plates, there is an axisymmetric current induced in the plates to push the plasma away. For the plasma current in the NSTX defined to be positive for standard co-injection operation, a negative current is thus

induced by the motion. The minimum plate current (i.e. a most negative value) during a disruption is plotted against the flat-top plasma current in figure 12, for the lower secondary plate in frame (*a*) and the lower primary passive plate in (*b*). As expected, the maximum induced current scales approximately linearly with the plasma current, with values of up to 70 kA observed.

During the current quench, the induced axisymmetric current is in the direction to replace the plasma current (i.e. is positive). The maximum plate current during a disruption, plotted this time against the pre-disruption plasma current, is shown in frames (*c*) and (*d*); a linear envelope is again observed. When these data are plotted against a quench-rate quantity such as $QR_{(80-20)}$, no clear trend is observed. This is to be expected from equation (1), as the time constant of the plate + support + vessel circuit is sufficiently longer than the I_P quench time that the maximum current is determined by the total linked flux. Interestingly, the quench-induced current is not larger in magnitude than that induced by vertical motion, demonstrating another case where the effects of plasma motion must be considered. However, the plasma motion induced forces will tend to push the plates towards the vessel, while the I_P quench-induced forces will want to pull the plates off their supports. Also note that there will be circulating currents in the plates, which will create overturning moments; these are not directly measured and so are not discussed here.

6. Conclusions

The purpose of this paper has been to document the features of the plasma current quench during disruptions in the NSTX. Our observations fall into two categories: the dynamics of the current quench itself and the dynamics of the local poloidal magnetic field time variations and eddy currents.

(i) Using the 80–20% quench rate definition, current quench rates up to $1.1\,\mathrm{GA\,s^{-1}}$ have been observed. These fastest quenches are typically best fit to linear waveforms. However, as was observed in JET [7], even slower current quenches often have periods with very rapid decay rates. As noted in previous work [17], the quench rates are faster in the NSTX than similar tokamaks at conventional aspect ratio; the difference is plausibly explained by the difference in the aspect ratio and the elongation of ST plasmas. Some weak correlation has been found between the $I_P(t)$ quench rate and the flat-top value of q^*, but in general, it is difficult to find relationships between the fastest current quenches and the pre-disruption equilibrium parameters.

(ii) The local poloidal field time variation at 10 locations around the poloidal circumference was studied as a function of the $I_P(t)$ quench rate, equilibrium geometry and plasma motion. The fastest field variations at the OBD are due to the current quench (i.e. the field time variation scales with the I_P quench rate) and occur in low-triangularity plasmas. At the midplane on the centrestack, the rate of increase in the poloidal field during the thermal quench can be comparable to the rate of decrease during the $I_P(t)$ quench.
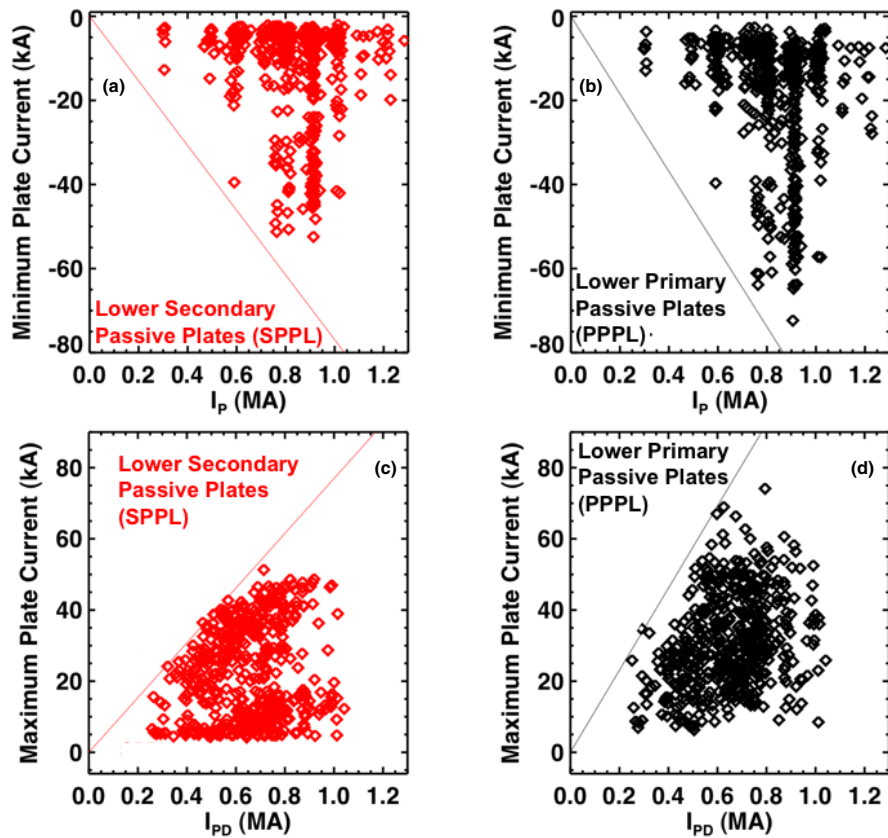
Figure 12. The minimum (top row) and maximum (bottom row) current induced in the lower secondary (*a*), (*c*) and primary (*b*), (*d*) passive plates. For plasma current defined to be in the positive direction, the minimum current is due to plasma motion towards the plates, while the maximum is due to the I_P quench.

(iii) Both vertical motion and the I_P quench induce nominally axisymmetric currents in the passive plate structures in the NSTX. Though these two sources drive currents in opposite directions, the magnitudes are comparable. These various conclusions reinforce the importance of integrated disruption modelling as described in [4, 5].

The results here are a first step to the characterization of disruption dynamics in the low aspect ratio NSTX plasma. As noted in section 2, the next step is the study of electromagnetic loading due to disruption halo currents. An array of magnetic pickup coils for measuring the toriodal field, and thus poloidal vessel currents [20], was installed for the 2008 run campaign; results from those studies will be presented in a future publication. It is equally important to expand the studies to include the dynamics of the disruption thermal quench. It is planned to use fast infrared thermography in the future to assess both the time-scale and spatial distribution of energy loss during the thermal quench. These additional measurements, coupled to further expansion of the NSTX operating space as a result of planned upgrades, should help to achieve a more complete understanding of disruption dynamics in an ST.

Acknowledgments

References

[1] Wesson J. 1997 *Tokamaks* (Oxford: Clarendon)
[2] Masaki K. *et al* 1995 *J. Nucl. Mater.* **220–222** 390
[3] Hender T.C. *et al* and the ITPA MHD 2007 Disruption and magnetic control topical group *Nucl. Fusion* **47** S128
[4] Riccardo V., Loarte A. and the JET EFDA Contributors 2005 *Nucl. Fusion* **45** 1427
[5] Sugihara M., Shimada M., Fujieda H., Gribov Y., Ioki K., Kawano Y., Khayrutdinov R., Lukash V. and Ohmori J. 2007 *Nucl. Fusion* **47** 337
[6] Sugihara M., Lukash V., Y Kawano, Yoshino R., Gribov Y., Khayrutdinov R., Miki N., Ohmori J. and Shimada M. 2003 *J. Plasma Fusion Res.* **79** 706
[7] Riccardo V., Barabaschi P. and Sugihara M. 2005 *Plasma Phys. Control. Fusion* **47** 117
[8] Rosenbluth M.N. and Putvinski S.V. 1997 *Nucl. Fusion* **37** 1355
[9] Dreicer H. 1959 *Phys. Rev.* **115** 23
[10] Harvey R.W., Chan V.S., Chiu S.C., Evans T.E., Rosenbluth M.N. and Whyte D.G. 2000 *Phys. Plasmas* **7** 4590
[11] Peng Y.K.M. and Strickler D.J. 1986 *Nucl. Fusion* **26** 769
[12] Ono M. *et al* and the NSTX Team 2000 *Nucl. Fusion* **40** 557

[13] Shimada M. *et al* 2007 *Nucl. Fusion* **47** S1 and references therein

[14] Menard J.E., Bell M.G., Bell R.E., Gates D.A., Kaye S.M., LeBlanc B.P., Maingi R., Sabbagh S., Soukhanovski V., Stutman D. and the NSTX National Research Team 2004 *Phys. Plasmas* **11** 639

[15] Gates D.A. and the NSTX National Research Team 2003 *Phys. Plasmas* **10** 1659

[16] Gates D.A. *et al* 2006 *Phys. Plasmas* **13** 056122

[17] Wesley J.C. 2006 Disruption characterization and databases activities for ITER *Proc. 21st Conf. on Fusion Energy (Chengdu)* (Vienna: IAEA) Paper IT/P1-21

[18] Strait E.J., Lao L.L, Luxon J.L. and Reis E.E. 1991 *Nucl. Fusion* **31** 527

[19] Granetz R.S., Hutchinson I.H., Sorci J., Irby J.H., LaBombard B. and Gwinn D. 1995 *Nucl. Fusion* **36** 545

[20] Riccardo V., Hender T.C., Lomas P.J., Alper B., Bolzonella T., de Vries P., Maddison G.P. and the JET EFDA Contributors 2004 *Plasma Phys. Control. Fusion* **46** 925

[21] Neyatani Y., Yoshino R., Nakamura Y. and Sakurai S. 1999 *Nucl. Fusion* **39** 559

[22] Counsell G.F., Martin R., Pinfold T., Taylor D. and the MAST team 2007 *Plasma Phys. Control. Fusion* **49** 435

[23] Knight P.J., Castle G.G., Morris A.W., Caloutsis A. and Gimblett C.G. 2000 *Nucl. Fusion* **40** 325

[24] Gates D., Menard J.E. and Marsala R.J. 2004 *Rev. Sci. Instrum.* **75** 5090

[25] Sabbagh S. *et al* and the NSTX Research Team 2001 *Nucl. Fusion* **41** 1601

[26] Gates D. 2006 *Nucl. Fusion* **46** 17

[27] Yoshino R., Nakamura Y. and Neyatani Y. 1996 *Nucl. Fusion* **36** 295

[28] Riccardo V. and the JET EFDA contributors 2003 *Plasma Phys. Control. Fusion* **45** A269–84

[29] Hofmann F. and Jardin S.C. 1990 *Nucl. Fusion* **30** 2013

[30] Sontag A.C. *et al* 2005 *Phys. Plasmas* **12** 056112

[31] ITER Physics Expert Group on Disruptions, Plasma Control, and MHD and ITER Physics Basis Editors 1999 ITER Physics Basis *Nucl. Fusion* **39** 2251

[32] Sugihara M. *et al* 2004 *Proc. 20th Int. Conf. on Fusion Energy 2004 (Vilamoura)* (Vienna: IAEA) CD-ROM file IT/P3-29 and http://www-naweb.iaea.org/napc/physics/fec/fec2004/datasets/index.html

[33] Humphreys D.A. and Whyte D.G. 2000 *Phys. Plasmas* **7** 4057

[34] Whyte D.G., Humphreys D.A. and Taylor P.L. 2000 *Phys. Plasmas* **7** 4052

[35] Humphreys D.A. and Kellman A.G. 1999 *Phys. Plasmas* **6** 2742

[36] Okamoto M. *et al* and JT-60 team 2008 *Proc. 22nd Int. Conf. on Fusion Energy (Geneva)* (Vienna: IAEA) CD-ROM file EX/7-2Rc